Proceedings of the ASME 2010 Eighth International Fuel Cell Science, Engineering and Technology Conference
FuelCell2010
June 14-16, 2010, Brooklyn, New York, USA

FuelCell2010-33328

NOVEL DYNAMIC QUASI-3-DIMENSIONAL HIGH TEMPERATURE FUEL CELL MODEL WITH INTERNAL MANIFOLDING

Dustin McLarty
National Fuel Cell Research Center, University of California Irvine
Irvine, CA, USA

Prof. Scott Samuelsen
Advanced Power and Energy Program, University of California Irvine
Irvine, CA, USA

Prof. Jack Brouwer
National Fuel Cell Research Center, University of California Irvine
Irvine, CA, USA

ABSTRACT

High temperature fuel cells have demonstrated potential for a wide array of energy applications while meeting future efficiency and emission targets. Earlier works captured either steady state performance of stacks or transient behavior of single cells. This work develops a model that can simulate and spatially resolve transient temperature, pressure and species distributions for a simulated fuel cell stack in a computationally efficient manner. The novel model accounts for internal manifolding of fuel and oxidant streams and predicts two dimensional fields associated with the dynamic operation of a single high temperature fuel cell. The MatLab-Simulink® model calculates dynamic performance for both solid oxide and molten carbonate fuel cells that utilize both direct and indirect internal reforming. This paper presents dynamic response characteristics to perturbations in power, fuel utilization and composition, and investigates control strategies that minimize PEN temperature variations and fluctuations during the transient responses. Air flow and inlet temperature controls are sufficient to control average PEN temperature, but internal heat transfer dynamics substantially change the spatial temperature distribution dynamics at different operational power densities.

INTRODUCTION

The U.S. Department of Energy has devoted significant effort towards technological breakthroughs for highly efficient low emission electricity production. Rising oil prices, the possibility of carbon taxation, and unnerving dependence on foreign energy sources stimulated the federal government's interest in clean energy sources that can meet new greenhouse gas emission targets. For years, fuel cells have promised high energy conversion efficiencies with extremely low pollutant emissions, but have been plagued by pitfalls common to many new technologies; poor economies of scale in manufacturing, complexity, durability, and lifetime cost. The combination of production advances and incentives have placed fuel cells on the cusp of widespread market penetration [1]. High temperature fuel cells have demonstrated remarkable performance in many stationary power applications [2] [3] [4]. This new technology must mature quickly to meet the demands of the marketplace. Market development occurs only once scientists and engineers have a foundation of understanding and experience with the rapidly emerging technology. Modeling is an effective means by which this experience and understanding can be garnered.

BACKGROUND

Molten Carbonate Fuel Cells (MCFC)

The first fuel cell type analyzed in this work, MCFC, typically consists of a high temperature molten salt electrolyte sandwiched between two nickel electrodes. These fuel cells typically operate in the temperature range of 550-650°C, and a current density range of .1-.25A/cm^2. Molten carbonate fuel cells have operated on methane, biogas [5], and syngas [6]. As a result, reformation of methane and other light hydrocarbons using high temperature steam coupled with water-gas-shift chemistry comprises an integral part of modeling molten carbonate fuel cells. Reformation kinetics for steam reformation of methane accompanied by water-gas shift is the

Nomenclature

A_{Cell}	Cell Area
ASR_{eff}	Effective Area Specific Resistance
D_h	Hydraulic Diameter
F	Faraday's Constant
h	Convection Coefficient
j	Current Density
k	Conduction Coefficient
$\dot{N}$	Flow Rate
P	Pressure
R	Rate of Reaction
R	Recirculation
T	Temperature
V	Volume

Greek Letters

X_i	Concentration of Species *i*
$X_{C_{XX}}$	Concentration of Carbon Containing Molecules
X_{H_2XX}	Concentration of H_2 Containing Molecules
η_{act}	Activation Polarization
η_{conc}	Concentration Polarization
η_{cath}	Cathode Polarization
η_{ohm}	Ohmic Polarization

Subscripts

A	Anode
C	Cathode
in	inlet
out	outlet

principle means for hydrogen or synthesis gas production [7]. Experimental results from Xu and Froment's work determined a single set of three global rate expressions that describe the kinetic processes between 675-1000°K. This temperature range satisfies the conditions in the reforming and anode channels of the fuel cells of this study.

Sheng et al. discovered that despite high operating temperatures MCFC are sensitive to small changes in peak temperature and temperature gradients. Excessive temperatures lead to rapid degradation, and large thermal gradients and fluctuations leads to physical fatigue and failure. A cascade control strategy can be employed to achieve optimal electrical production during load fluctuations [8]. The inability of most commercial MCFC systems to measure internal stack temperature distributions limits the application of this strategy.

MCFC models often use bulk parameters to increase computational efficiency, sacrificing the accuracy of a spatially derived model [9]. Brouwer, et al. compared overpotential terms derived from the Nernst equation to those of an agglomerate model proposed by Yuh and Selman. The latter appeared to more accurately represent the operating voltage at the low current densities studied.

Solid Oxide Fuel Cells (SOFC)

The second type of high temperature fuel cell considered in this work is the SOFC. These fuel cells typically comprise a yittria-stabilized zirconia electrolyte, or similar ceramic material, that conducts oxygen ions [10]. Hydrogen, natural gas or a coal derived syngas can directly fuel SOFC systems. This type of fuel cell is being investigated for a very wide range of applications; small distributed generation, large grid-connected power generation, and auxiliary power units aboard naval, land and aerospace vehicles [11] [12]. These applications will often require fast transient load following capability, an historical weakness of fuel cell systems to-date [13]. The work of Mueller et al. investigated three different mechanisms that each contribute to SOFC transient behavior at different time scales. The electrochemistry of the FC can react to transients on the order of milliseconds, but the redistribution of species through the system can occur over several seconds due to the low velocities of the air and gas streams. Temperature transients require even greater amounts of time, often minutes or hours, depending upon the size of the stack.

Temperature distributions largely depend upon internal reforming characteristics of these high temperature fuel cells when operated on hydrocarbon fuels. Experiments conducted with an operating SOFC short stack have demonstrated the fuel flexibility and internal reforming characteristics of SOFC technology [11]. Different steam-to-carbon ratios and methane concentrations change the cooling impact of internal reformation as well as Nernst potential and local electrochemical losses.

MODEL DESCRIPTION

A spatially- and temporally-resolved fuel cell model has been developed using the MatLab Simulink® interface. The model incorporates necessary terms for both MCFC and SOFC simulations and is derived from first principles. Fuel Cell Energy's (FCE) Direct Fuel Cell® (DFC) provides the basis for the MCFC design with specialized reformer cells spaced in between each ten active fuel cells. A generic planar SOFC design with scalable active area and the option for internal and/or external reforming is simulated. Counter flow and cross flow configurations with a 5 by 5 nodal grid were tested in this study; higher resolutions are possible with significant additional computing cost. The design of the current model applies to generic or specific fuel cells including the DFC line from FCE and scales to represent any planar type MCFC or SOFC.

Spatial resolution allows for analysis of the internal temperature profile and thus internal heat transfer must be modeled with precision. The analysis allows for local evaluation of Nernst potential and losses with local conditions of pressure, temperature, and species. Internal reforming rates are evaluated locally and local heat generation calculated from the difference in chemical potential energy and local electrical power production. This provides significant improvement in accuracy over a bulk model, particularly in the task of scaling and control, but also for accurately determining performance capabilities. Bulk model parameters must be tuned for a particular cell, and don't scale effectively with dimensional parameters or changing cell characteristics due to the differences in heat transfer, conduction and diffusion

coefficients and distances. Bulk models cannot accurately determine performance limitations due to any variable that has significant spatial variations in real fuel cell systems (e.g., temperature, species concentrations).

A modeling methodology suitable to evaluate the performance, integration and control of high temperature fuel cells has been previously developed and effectively utilized at the University of California, Irvine. The modeling methodology was developed to evaluate the transient performance, and system interactions of integrated high temperature fuel cell systems [9] [13] and fuel cell - gas turbine hybrid systems [14] [15] [16]. The modeling methodology is based upon the quasi-dimensional discretization of fuel cells into control volumes. Within each component control volume the temperature, species mole fractions, pressure and other characteristics are evaluated by solving dynamic conservation of mass, energy and momentum equations as required. From the resolved temperature, species mole fractions and pressure; transport phenomena (e.g., heat transfer, and species diffusion) and chemical reactions can be evaluated to determine the performance of each energy system component. Developed models of energy system components are then integrated to form models of complex integrated energy systems that contain multiple energy system components, all with resolution of individual system component physics, chemistry and electrochemistry. By simultaneous solution of the dynamic equations, complex and coupled interactions amongst system components are captured.

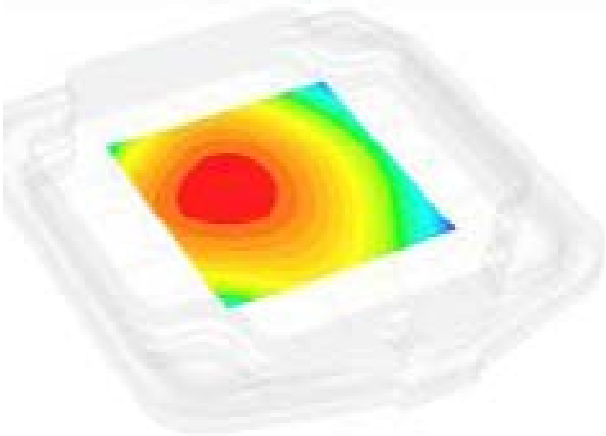

Figure 1 FCE Spatial Temperature Profile

The current work extends the methodology by integration of pre- and post heating manifolds into the stack configuration representing a novel modeling approach. This innovation captures the physics coupling internal manifolding to performance characteristics and temperature distributions of a fuel cell stack. This is achieved through the description of a simplified manifolding geometry wherein the incoming air and fuel streams flow past the stack edges prior to entering the active cell area and after exiting the active cell area. Figure 1 shows a steady state cross flow temperature distribution from Fuel Cell Energy and Figure 2 compares that to a profile generated by the novel model developed in this study. The spatially resolved temperature profiles clearly demonstrate similar temperature gradients and local temperature distribution within the active cell area.

The flow configuration along the edges represents a simplified internal manifolding geometry for a fuel cell stack configuration. This allows for the incorporation of energy transfer directly from the stack to the incoming air and fuel streams without modeling a large stack and surrounding vessel. The justifications that this geometric simplification captures the thermodynamic coupling under steady state and dynamic conditions are as follows.

- Thermal energy generated in the cell preheats the inlet air and fuel streams between 50 and 150°C before entering the cell, as per real stacks.
- The final cathode exhaust stream temperature closely mirrors that of the peak PEN temperature, and is not the source of energy for internal pre-heating.
- The spatial temperature profile of the PEN closely matches that of Fuel Cell Energy's cross flow cell.
- Internal flow, at low Peclet numbers, advects all heat in the fluid toward the exhaust stream. Energy mobility upstream exists only in the solid components; electrolyte and bipolar plate. Extremely high convective and radiation heat transfer in the manifolding results in conduction limited heat transfer to the incoming gas streams.

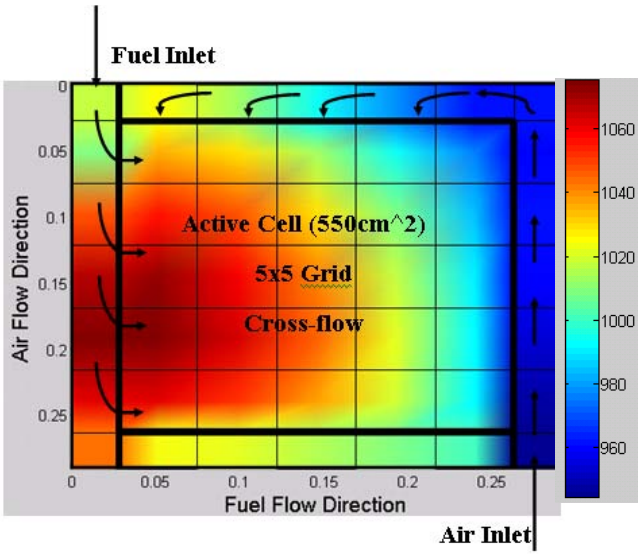

Figure 2 NFCRC Model Temperature Profile

The spatial temperature profiles presented in Figure 1 and Figure 2 represent the SECA target goals for the SOFC case of 100°C temperature rise, 500mW/cm^2 power density, and a fuel utilization of 80%. This method captures the extremely important coupling effect of operating power density and internal pre-heating. With constant air flow, additional power/ heat generation will increase the pre-heat and PEN temperature gradient. However, with variable air flow, additional

power/heat generation requires more air to maintain constant average PEN temperature. The additional airflow reduces pre-heating and increasing the gradient across the cell when cathode inlet and outlet temperatures are controlled. Higher inlet temperatures at high air flow, achieved through recirculation heating, can possibly correct for varying internal pre-heating and maintain fixed PEN temperature gradients at higher power production. This important coupling effect must be captured for correct dynamic analyses and control studies. Many control strategies assume the cell inlet temperatures can be controlled precisely, yet do not account for the variable internal pre-heating. The strategy employed in this study is a novel method of simulating the interaction between air flow rate and internal pre-heating.

The spatial resolution is achieved by dividing a single cell into 25 nodes, and each node into five distinct components; the oxidant separator plate, the cathode gas stream, the electrodes and solid or molten electrolyte, the anode gas stream, and the fuel separator plate. These five layers comprise a single cell, and in the case of Fuel Cell Energy's Direct© internally reforming MCFC, these are grouped into stacks of ten separated by a reformer plate. These five layers isolate many of the physical and chemical processes yielding simple first principles modeling of the species reformation, local pressure, current density, heat generation, and mass transfer across the electrolyte. This internal geometry models 125 control volumes to capture the internal heat transfer via convection from electrolyte and separator plates to gas flows, via conduction between electrolyte and plates and via conduction between nodes of each of the solid layers.

MODEL DEVELOPMENT

Species Conservation

The following equations account for the change in species occurring in each node of the fuel cell anode and cathode compartments. The expression represents continuity through a control volume species balance. The expression assumes a perfectly stirred reactor with the exit conditions representing the concentrations throughout the control volume.

$$\frac{R_{REF} + R_{USE} + \left(\dot{N}X\right)_{in} - \left(\dot{N}X\right)_{out}}{\frac{P_j V_j}{R_U T_j}} = \frac{dX_i}{dt} \qquad (1)$$

The consumption rates for the cathode and anode gases are based upon the two half reactions for a molten carbonate and solid oxide fuel cell. The reaction rate is arranged in an array of seven species specified below. A positive reaction rate indicates the production of that species while a negative rate indicates consumption, where i is the local current and F is Faraday's constant.

$$species = [CH_4 \quad CO \quad CO_2 \quad H_2 \quad H_2O \quad N_2 \quad O_2]$$

Table 1. Fuel Cell Reaction Vectors

HT-FC	Molten Carbonate	Solid Oxide
$\boldsymbol{R_{Cathode}}$	$\left[0\,0\ \frac{-1\cdot i}{2F}\ 0\,0\,0\ \frac{-1\cdot i}{4F}\right]$	$\left[0\,0\,0\,0\,0\,0\ \frac{-1\cdot i}{4F}\right]$
$\boldsymbol{R_{Anode}}$	$\left[0\,0\ \frac{1\cdot i}{2F}\ \frac{-1\cdot i}{2F}\ \frac{1\cdot i}{2F}\,0\,0\right]$	$\left[0\,0\,0\ \frac{-1\cdot i}{2F}\ \frac{i}{2F}\ 0\,0\right]$

The fuel utilization factor is calculated on the basis of fuel flow rate which is controlled (through a PID feedback controller) in the current model to supply sufficient hydrogen to meet the instantaneous current. The following expressions determine fuel flow rate and fuel utilization.

$$Util_{fuel} = \frac{H_{2,consume}}{H_{2,avail}} \qquad (2)$$

$$H_{2,consume} = \frac{n_{cell} \cdot j \cdot A_{Cell}}{2 \cdot F} \qquad (3)$$

$$H_{2,avail} = \dot{n}_{fuel} * \left(4 \cdot \chi_{CH_4} + \chi_{CO} + \chi_{H_2}\right) \qquad (4)$$

Air utilization is calculated by comparing the oxygen supplied and consumed. Air flow is controlled by a separate PID controller based upon the measured air inlet and fuel cell exhaust stream temperatures (not air utilization). Higher air utilization implies a more efficient fuel cell that requires less cooling air. At very high air utilization local Nernst potential decreases significantly as the partial pressure of oxygen diminishes in downstream nodes.

Reformation and Water-Gas Shift

The internal and external reformation of methane as well as water gas shift chemistry calculations in the model are based upon the well established kinetic reaction mechanisms outlined by Xu and Froment in their two part 1989 paper. These authors outlined three reactions involved in the production of hydrogen from methane and water, and measured the rate parameters associated with each.

$$CH_4 + H_2O \rightarrow CO + 3H_2 \qquad (5)$$

$$CO + H_2O \rightarrow CO_2 + H_2 \qquad (6)$$

$$CH_4 + 2H_2O \rightarrow CO_2 + 4H_2 \qquad (7)$$

Reformation occurs in the anode compartment, and is a function of the local pressure, temperature, and species. The presence of catalyst material on the anode surface also plays a role in the reformation kinetics and local heat transfer.

$$R_{REFORM} = f(P, T, \chi_{out}) \qquad (8)$$

Conservation of energy applies to each cell component resulting in a detailed heat transfer model for each node. Local conditions and material properties are used to estimate conduction between the three solid layers of each node and adjoining nodes, and convection between the solid layers and gaseous flows. The molten carbonate design includes a reformer cell spaced between each ten active cells. The

reformer cell acts as a heat sink, providing a significant portion of the internal stack cooling.

Table 2 presents several intrinsic and extrinsic properties of the stack and the anode, cathode, and electrolyte material properties that complete the physical description of the FC model included in the current study. Each of these may be modified to calibrate the model to any particular fuel cell design.

Table 2. Fuel Cell Parameters

Component	Parameter	Unit	MCFC	SOFC
Stack	Length	m	1.2	.25
	Width	m	0.8	.25
Bipolar Plate	Thickness	m	0.02	0.006
	Density	kg/m^3	7900	1975
	Specific Heat	J/kg*K	611	611
	Conductivity	W/mK	25.4	25.23
Anode	Channel Height	m	0.004	0.002
	Channel Width	m	0.004	0.005
	Wall Thickness	m	0.005	0.002
Cathode	Wall Thickness	m	0.005	0.002
	Channel Height	m	0.006	0.002
	Channel Width	m	0.006	0.005
Electrolyte	Membrane Thickness	m	0.001	18e-6
	Cathode Thickness	m	N/A	800e-6
	Anode Thickness	m	N/A	50e-6
	Density	kg/m^3	2702	375
	Specific Heat	J/kgK	1146	800
	Conductivity	W/mK	218	6.19
Reformer	Channel Height	m	0.005	N/A
	Channel Width	m	0.003	N/A
	Wall Thickness	m	0.001	N/A

Overpotentials/Voltage Losses

Molten Carbonate

The molten carbonate voltage calculations use expressions for three traditional loss terms, activation, Ohmic and concentration. The Butler-Volmer equation, the fundamental equation of electrochemical kinetics, encapsulates activation polarization. The simpler Tafel expression approximates the B-V equation at moderate to high current densities.

$$\eta_{act} = -\frac{RT}{\alpha nF}\ln j_0 + \frac{RT}{\alpha nF}\ln j \qquad (9)$$

The effective resistance modeled in these experiments is taken from the empirical test cell data gathered by Rivera of UCI, and follows correlation 10.

$$ASR_{eff} = C_2 + C_1 * T \qquad (10)$$

$$\eta_{ohm} = j \cdot ASR_{eff} \qquad (11)$$

Concentration losses arise from diffusion limitations of reactant gases to the reaction sites and product gases from the reaction sites. Production of electrical current requires continual supply (replenishment) of reactants to the triple phase boundary (TPB), however, at some currents reacting species cannot diffuse through the electrode quickly enough. Reactant concentration affects the fuel cell performance through the Nernst potential and through the reaction kinetics. Reaction kinetics also depends heavily upon reactant concentrations at the TPB. These mechanisms are summarized in an expression for the net concentration loss in a form similar to the Tafel expression.

$$\eta_{conc} = \left(1 + \frac{1}{\alpha}\right)\frac{R_U T}{2F} ln \frac{j_L}{j_L - j} \qquad (12)$$

Table 3. Voltage Loss Parameters for MCFC

Physical property	Variable	Value	Units
Limiting Current Density	j_l	4000	Amps/m^2
Curve Fit Term 1	C_1	6.667x10^{-7}	Ohm-m^2/K
Curve Fit Term 2	C_2	4.783x10^{-4}	Ohm-m^2
Charge Transfer Coefficient	α	.4	none
Exchange Current Density	j_o	50	Amps/m^2

Solid Oxide

Evaluation of the Nernst potential in the free stream and at the TPB yields the following loss expression on the cathode electrode.

$$\eta_{cath} = \frac{R_U T}{4F} ln \frac{j * c_R^*}{j_L * c_R^0} \qquad (13)$$

The ratio of species concentrations can be defined in terms of the local pressure, free stream concentration, current density, and diffusivity rate as follows.

$$\frac{c_R^*}{c_R^0} = \frac{1}{P^C\left\{x_{O_2|d} - t^C j\, RT/\left(4FP^C D_{O_2,N_2}^{eff}\right)\right\}} \qquad (14)$$

Having accounted for both activation and concentration losses with the previous expression, all that remains to be found is the Ohmic loss. As with the MCFC, the Ohmic resistance will be calculated using area specific resistance. ASR is dependent upon the membrane thickness, electrolyte temperature, and conductivity.

$$\eta_{ohm} = j * \frac{t^M T}{Ae^{-\Delta G_{act}/(RT)}} \qquad (15)$$

Table 4. Solid Oxide Overpotential Parameters

Physical Property	Variable	Value	Units
Effective Oxygen Diffusivity	D_{O_2,N_2}^{eff}	$2\ x\ 10^{-5}$	(m^2/s)
Transfer Coefficient	α	0.7	$(none)$
Exchange Current Density	j_0	1	(A/cm^2)

Electrolyte Constant	A	$13\ x\ 10^7$	$(K/\Omega \cdot m)$
Electrolyte Activation Energy	ΔG_{act}	100	(kJ/mol)
Electrolyte Thickness	t^M	18	μm
Anode Thickness	t^A	50	μm
Cathode Thickness	t^C	800	μm

Convection Coefficient

Calculation of the local convective heat transfer relies on the assumptions of fully developed flow and uniform surface temperature in each node. The following Nusselt number expression was used to calculate the convection coefficient using the thermal conductivity of the gas, *k*, and a hydraulic diameter, D_h, for the channel. From standard engineering tables the Nusselt number was found to be approximately 4.

$$Nu_D = \frac{hD_h}{k} \tag{16}$$

Cathode Inlet Composition

The composition of the cathode inlet stream plays a significant role on the overall performance of the cell. A reduction in oxidant concentration at the cell inlet reduces oxidant partial pressure throughout the cell. This negatively impacts the local Nernst potential and loss terms, thereby producing more heat and reducing the efficiency of the cell. Cathode recirculation, if present, can increase or decrease the oxidant concentration at the inlet. Cathode recirculation diminishes oxygen concentration when diluting ambient air, but increases CO_2 concentration which benefits an MCFC.

Molten Carbonate

A molten carbonate fuel cell recycles CO_2 from the anode compartment and post combustor into the cathode inlet stream. The anode off gas is diluted with atmospheric air, and the resulting inlet species concentration are calculated. The following expressions determine the inlet concentrations.

$$X_{CO_2} = \frac{\{\dot{n}X_{CXX}\}_{A,out} + \boldsymbol{R}(\dot{n}X_{CO_2})_{C,out}}{\{\dot{n}\}_{C,in}} \tag{17}$$

$$X_{H_2O} = \frac{(\dot{n}X_{H_2XX})_{A,out} + \boldsymbol{R}(\dot{n}X_{H_2O})_{C,out}}{\{\dot{n}\}_{C,in}} \tag{18}$$

$$X_{O_2} = \{X_{O_2}\}_{Air}\left(1 - \frac{\{\dot{n}(1+2X_{CH_4})\}_{A,out}}{\{\dot{n}\}_{C,in}}\right) \tag{19}$$

$$X_{N_2} = 1 - X_{O_2} - X_{H_2O} - X_{CO_2} \tag{20}$$

Solid Oxide

The solid oxide fuel cell model employs ambient air containing only oxygen and nitrogen as an oxidant stream. The re-circulated gas stream will also primarily consist of oxygen and nitrogen with lower oxygen content. Equations 21 and 22 represent the expressions for the inlet species concentration of the SOFC cathode.

$$X_{O_2} = (1 - \boldsymbol{R})\{X_{O_2}\}_{Air} + \boldsymbol{R}\{X_{O_2}\}_{C,out} \tag{21}$$

$$X_{N_2} = 1 - X_{O_2} \tag{22}$$

STEADY STATE PERFORMANCE RESULTS

Initial model testing and validation relied on a parametric variation of key design parameters including fuel utilization, average operating temperature, PEN temperature gradient, and power density. The MCFC model was also used to investigate the impact of CO_2 concentration and steam-to-carbon ratio. The results of the subsequent section demonstrated the robustness of the novel model design in simulating physical phenomena and garnered key insights into behaviors not apparent through study of the fundamental equations. The data presented employed a cross-flow configuration, but similar results obtained for the counter-flow configuration demonstrate temperature profile and current distribution as the primary differences between the arrangements. This parametric analysis was conducted by controlling the stack voltage with a feedback loop to converge on the desired power density. A second controller adjusted the rate of oxidant supply to achieve the desired stack temperature rise, and a final controller adjusted the temperature of the fuel and oxidant inlet streams to maintain a fixed average PEN temperature. Twenty-nine system parameters were recorded for each operating condition.

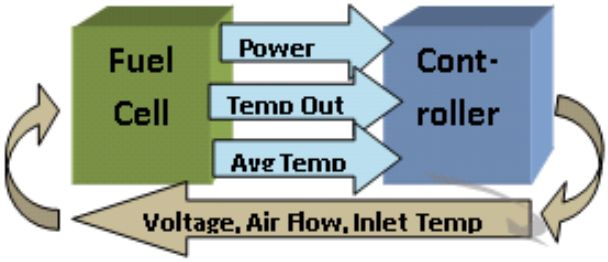

Figure 3 Fuel Cell Control Strategy

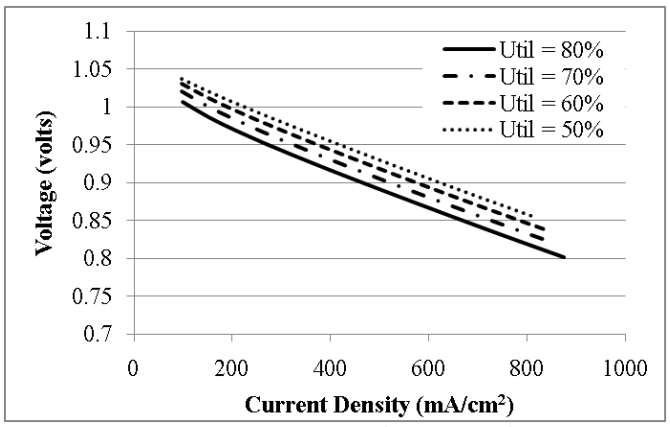

Figure 4 SOFC V-I Curves at 750°C and 200°C Gradient

Variation of fuel utilization was found to significantly impact cell performance. Figure 4 demonstrates the inverse relationship between voltage and current as well as voltage and fuel utilization. Lower fuel utilizations yield higher fuel concentrations at the anode exit resulting in increased Nernst potential throughout the cell. The increased cell voltage improves local efficiency at the cost of additional unspent fuel. The un-utilized fuel proportionally diminishes system performance unless some form of anode recirculation is employed. The extremely low current density regime is not shown in these figures because the cell operates so efficiently in this regime that it is difficult to maintain a substantial temperature gradient across the cell. The thermal requirements for cooling air do not supply enough oxidant to meet the reaction needs. The cathode concentration loss does not increase until oxidant utilization is nearly 100%, where the voltage curve is extremely steep, making numerical solutions difficult. The figures do not depict the high current regime because, as the voltage reaches the peak of the power density curve, two solutions exist for a power controlled model. Controlling voltage rather than power allows lower voltage operating conditions to be investigated.

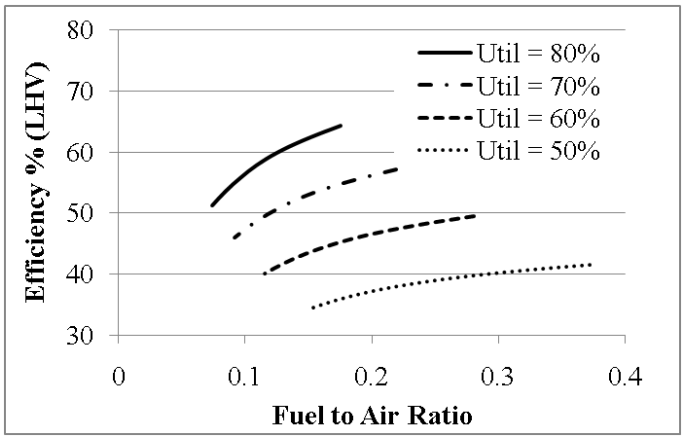

Figure 5 SOFC Efficiency vs. Fuel to Air Ratio

Lower fuel utilizations reduce losses and raise total cell voltage. Despite this benefit, system efficiency drops due to the additional unused fuel. Figure 5 shows a strong correlation between efficiency and fuel to air ratio. When losses are reduced the air flow requirement decreases, simultaneously raising both efficiency and fuel to air ratio. Lower fuel utilizations increase the fuel to air ratio, and reduce losses, but do not necessarily increase efficiency. Under certain circumstances when the FC employs anode recirculation, produces usable hydrogen, or pairs with a heat engine using the excess fuel, some benefits to lower utilization exist. MCFC see an additional benefit of higher inlet CO_2 concentration at higher fuel to air ratios, resulting in optimal utilizations that are lower than that for SOFC.

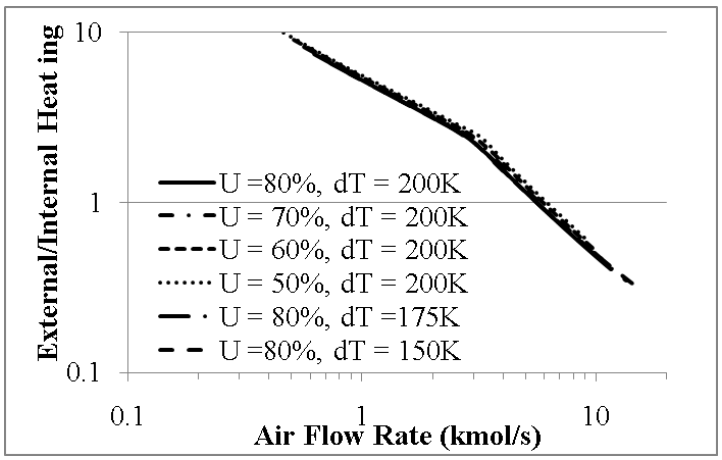

Figure 6 Log-Log Plot of Heating Ratio vs. Air Flow Rate

The model employed demonstrates the novel capability of capturing the coupled effects of air flow rate, power density and internal heating by capturing the physics of internal manifolding as discussed previously. The air flow rate into the FC is controlled to obtain a 200°C temperature rise from inlet to outlet, thus as the PEN temperature gradient decreases the manifolding temperature rise increases. The amount of pre-heating achieved by the internal manifolding is not constant, and will be reduced with increasing air flow. Many factors including fuel utilization, cell temperature gradient, and power density affect the flow rate of cooling air supplied to the stack to maintain a fixed operating temperature. Figure 6 shows air flow rate is entirely responsible for the ratio of internal temperature rise and external pre-heating. Moreover it is shown to exhibit a linear trend on a log-log plot. The geometry described results in a shorter manifolding residence time at higher flow rates. This results in reduced heat transfer to the incoming air, lowering the cell inlet temperature. In response, the temperature gradient increases to sustain a fixed operating temperature difference from entrance to exit.

Figure 7 shows the correlation between rising temperature gradients and higher power densities, corresponding to higher air flow rates, and lower cell inlet temperature. Figure 7 would seem to indicate a cooling impact of reduced fuel utilization, but that is not the case. The lower fuel utilization corresponds to a higher operating voltage, and thus a reduced air flow. Figure 6 clearly demonstrated air flow rate as the only contributor to temperature gradient. The shift in the trend of each line is due to the movement of the peak location in the cell temperature profile. With the cell descretized into 25 nodes this corresponds to a shifting of the peak from the last node in the airflow direction to the second to last node.

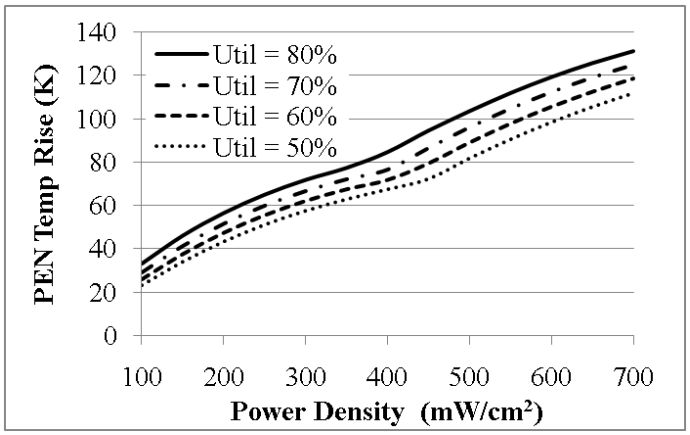

Figure 7 SOFC Stack Temperature Gradient vs. Power Density and Fuel Utilization

Figure 8 presents simulation results for variations in stack temperature rise. The heat generation of the stack depends upon the power density and efficiency, and the majority of the generated heat is convected from the cell into the cathode stream. The PEN temperature profile closely follows that of the cathode gas due to the large surface areas and low Reynolds number flow of the cathode compartment. The air flow rate entering the cathode and the heat generation determine the cell temperature rise.

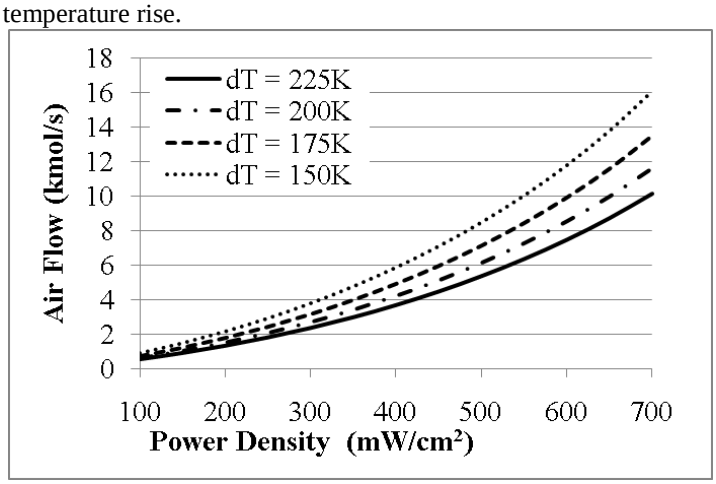

Figure 8 Cooling Air Requirements at Varying Operational Power Densities

Figure 8 indicates the inverse relationship between air flow and temperature rise. A greater airflow and the same heat production, yields lower temperature increases. The impact of reduced power density with constant air flow can be seen to move laterally to the left onto curves with lower temperature gradients. The temperature rise produced little effect on the performance curves of the cell with fixed average PEN temperature. The fuel cell requires exponentially more air flow to maintain smaller thermal gradients.

Simulation results indicate PEN temperature gradient and peak PEN temperature depend upon three operational parameters; power density, fuel utilization, and stack temperature rise. The temperature profile of a HT-FC plays a large role in degradation mechanisms, and thus maintaining a constant temperature profile, especially during transients, can vastly improve the longevity of the fuel cell. This study shows that controlling the average PEN temperature by fixing the stack inlet and outlet temperature differential may be insufficient to maintain a constant temperature profile through any significant operating range.

The carbon dioxide inlet concentration and steam to carbon ratio studies presented in Figure 9 through 12 relate only to MCFC. Carbon dioxide concentration depends on the anode off-gas composition and the ratio to diluting ambient air for systems that incorporate anode off gas as the CO_2 source for the cathode inlet stream. The exact expressions for inlet composition were presented in the model development section. Cathode recirculation can supply additional CO_2 for FC-GT hybrids, with recirculation requirements determined by pre-heating and turbine temperature requirements. Figure 9 demonstrates the positive impact of higher CO_2 inlet concentrations. A strong correlation exists between inlet CO_2 concentration and FC efficiency.

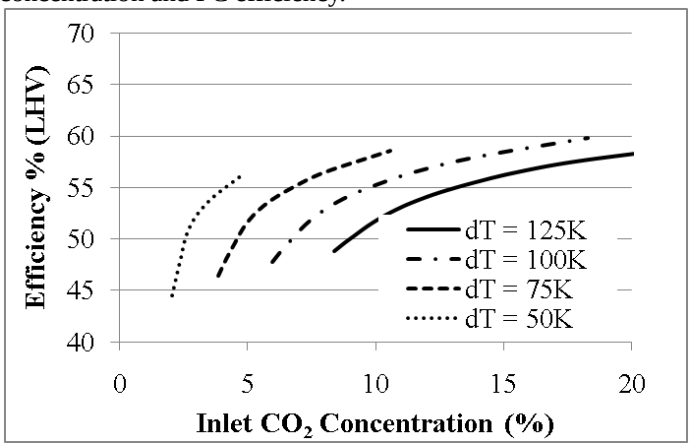

Figure 9 MCFC Efficiency vs. Inlet CO_2 Concentration

The benefit of re-circulating more CO_2 reduces as CO_2 concentration increases. The additional heat capacity of CO_2 reduces cooling requirements, as does the reduced heat generation from more efficient operation stemming from a greater diffusion of CO_2 to the reactant sites; a potential boon to hybrid systems, whose performance depends heavily on the amount of cooling air. Figure 10 demonstrates the direct relationship between fuel to air ratio and inlet CO2 concentration in MCFC with no cathode recirculation. This relationship can be exploited in hybrid systems by operating at lower fuel utilizations to boost the fuel to air ratio. This relationship can also be exploited in co-generation systems producing usable hydrogen as a byproduct.

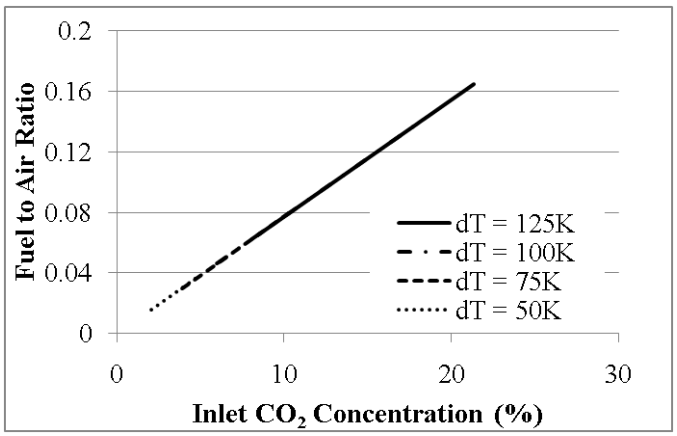

Figure 10 MCFC Fuel to Air Ratio vs. Inlet CO2 Concentration

Some studies suggested controlling the steam ratio as a means of temperature control for MCFC systems. This study supports these claims, demonstrating a slight reduction in peak electrolyte temperature at higher steam concentrations. The cathode gas stream still accounts for most of the stack cooling, but the increasing steam concentration reduces the high current region near the fuel entrance that produces the highest temperature throughout the cell. The increased steam also promotes a more complete reformation of the methane feedstock, producing more hydrogen and raising overall cell voltage. This effect ceases above a steam to carbon ratio of 3.0 when near complete methane reformation occurs.

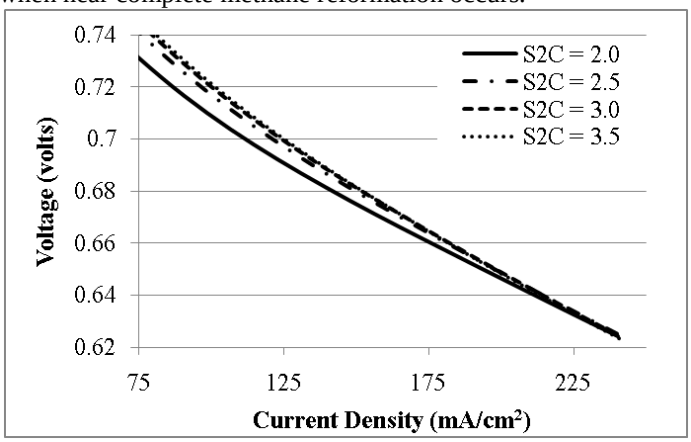

Figure 11 MCFC V-I curve vs. Steam/Carbon Ratios

Figure 11 and Figure 12 present data with varying steam to carbon fuel ratios. Figure 11 shows a slight reduction in voltage as the steam to carbon ratio increases from 2 to 3.5. Higher steam to carbon ratios reduce the likelihood of coking, but eventually become detrimental to performance as the partial pressure of fuel is diminished. This study indicates optimal operation occurs near a steam to carbon ratio of 3. Additional water in the fuel stream increases the thermal capacitance of the anode gas and provides some additional cooling to the stack, as does the increased internal reformation. This is supported by the data presented in Figure 12, but the primary reason for the reduction in peak temperature is the reduction of the localized peak temperature near the fuel entrance region. The high temperature associated with this region is due to the high current density resulting from high fuel concentration, and the gradient depends upon the material thickness and thermal conductivity properties.

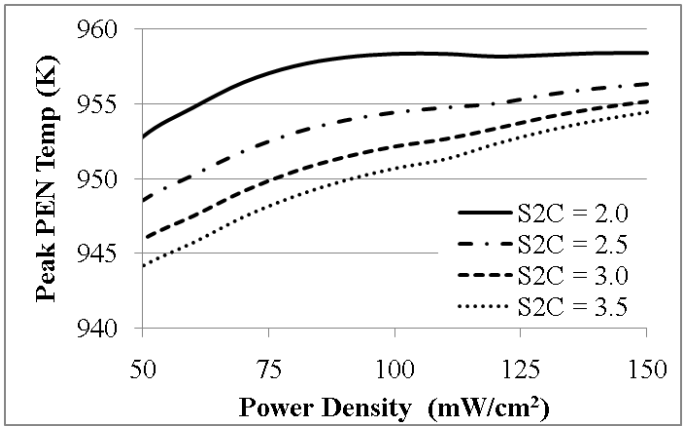

Figure 12 MCFC Peak Temperature vs. Power Density and Steam to Carbon Ratio

DYNAMIC RESULTS

The model described in this paper was derived and implemented in the Matlab-Simulink® interface for dynamic calculations. This enabled the study of different control strategies for temperature management in complete systems. The analysis described here presents FC responses to different perturbations as a means of validation prior to implementing control strategies. The response analysis will generate insights into relative impacts of different perturbations and indicate which induce operation limits or require specific controls. Each study began from a design case with parameters and operating conditions listed in tables 2-5.

Table 5 Fuel Cell Parameters

Parameter	Case 1	Case 2	Units
Power Density	500	200	mW/cm^2
Voltage	0.8685	0.9702	Volts
Current	316.64	113.34	Amps
Fuel Utilization	80%	80%	
Fuel Species	[.0049 .0262 .0378 .91 .0001 .021 0 .149]	same	
Oxidant Species	[0 0 0 0 0 .81 .19]	same	
Fuel Flow	0.149	0.0536	kmol/s
Air Flow	7.391	1.8329	kmol/s
PEN T_{avg}	1023	1023	Kelvin
Cath T_{in}	875.67	840.7	Kelvin
Cath T_{out}	1054.7	1039.1	Kelvin

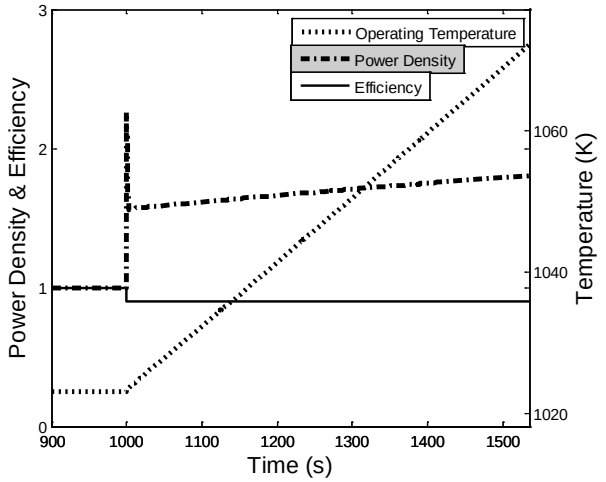

Figure 13 Fuel Cell Response to a Step Decrease In Voltage

The first perturbation, shown in Figure 13, was a step change in voltage from 0.9683 to 0.8683. The sudden voltage drop and accompanying fuel increase to maintain 80% utilization, raised power density 60% from 200mW/cm^2 to nearly 320mW/cm^2 in a matter of seconds. The initial spike visible in Figure 13 results from a momentary period of high current before the as the fuel concentration reaches a new equilibrium. The higher power density produces additional heat that begins to steadily raise the stack temperature by .1°C/s. The rising temperature reduces ohmic losses; gradually raising the power output to 380mW/cm^2.

Efficiency, closely related to voltage, drops instantly and remains fixed at 90% of pre-transient efficiency. Considering temperature as the primary transient of concern throughout power fluctuations, control of the air flow rate and inlet temperature should sufficiently maintain stack integrity. The relationship between air flow and power density, Figure 8, is non-linear, multi-variable dependant, and requires novel feedback controls to minimize temperature fluctuations. Figure 13 demonstrates the slow thermal response for rapid ramp up of power output. Temperature tolerances of 10°C would not be exceeded for 100s, sufficient time for a novel feedback controller in an integrated system to meet the new air flow demand.

The second perturbation, shown in Figure 14, was a step change in fuel utilization from 80% to 60% at fixed voltage and air flow. Higher fuel concentrations throughout the anode compartment allow for higher reaction rates, producing more current, and thus more power at the fixed voltage operation. The new power output increases the heat generation and thus the temperature, though at a significantly slower rate than previously. Fuel utilization largely impacts efficiency by determining the amount of fuel that goes unused by the FC.

Efficiency depends primarily upon fuel utilization, as any unused fuel produces no power, only heat. When available heat already provides sufficient energy for pre-heating the inlet air stream, higher fuel utilizations result in higher efficiencies, until concentration losses become a significant factor at extremely high utilization.

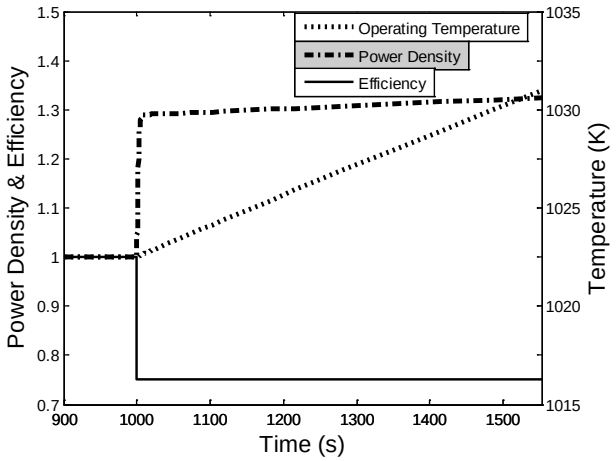

Figure 14 Step Decrease in Fuel Utilization

Figure 14 demonstrates an interesting aspect of fuel cell technology, the potential to perform above design power for several minutes purely by increasing fuel flow. Novel dynamic control of the fuel utilization factor could manipulate fuel flow for operational benefit. Applied in a load following scenario with very short peak power demands this feature would allow a system to be undersized by as much as 30% and still meet the peak demand for several minutes before significant temperature rise jeopardizes the stack. This power boost comes at significant loss of efficiency, but would be expected to only rarely be employed for peak demands.

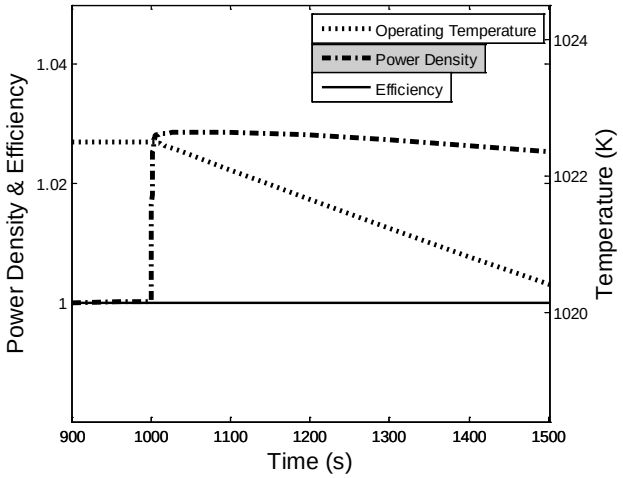

Figure 15 10% Increase in Air Flow Rate

The third perturbation, shown in Figure 15, was a sudden 10% increase of the air flow rate. A small, 2.5%, but very rapid rise in current produces the increase in power seen in Figure 15. However, the subsequent decrease in operating temperature, from the increased cooling capacity of the air, increases cell resistance, reducing current, power, and heat generation. Lower heat production results in positive feedback,

further reducing the temperature and power. Efficiency remains steady, as it depends on voltage and fuel utilization, both of which were held fixed in this study. The impact of increasing air flow in combination with fuel flow, as in the previous example, allows operation above rated power for sustained periods of time with little or no thermal fluctuation. Above rated power operation does significantly reduce efficiency.

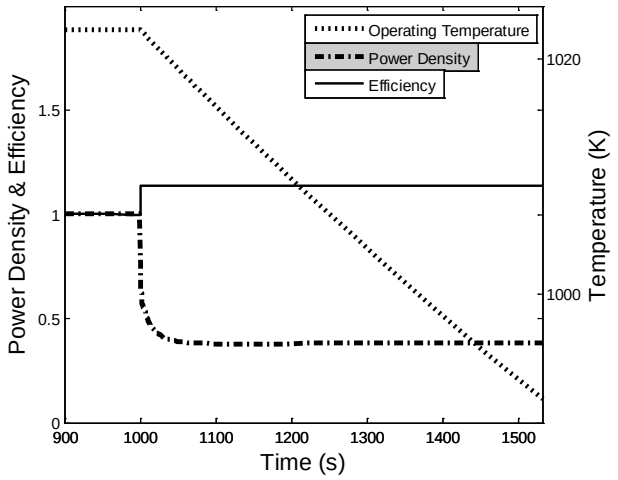

Figure 16 Step Change in Fuel Composition

The fourth perturbation, shown in Figure 16, was a sudden change in fuel composition from a low methane to high methane concentration syngas; <1% to 17%. Power quickly drops nearly 60% due to the lower hydrogen content in the anode compartment. The increased internal reformation increased internal cooling, thereby reducing FC temperature, increasing area specific resistance, and further reducing the power output. Efficiency rises due to the lower heating value of the higher methane concentration syngas. The stack cooling can be compensated by a reduction in the air stream flow rate or voltage. Fuel cells perform best with high hydrogen content fuel streams, however, when such a feedstock is unavailable, efficient operation at lower power densities is possible.

The first three perturbations each impact the FC operation differently, and can be independently controlled. The impact of any one perturbation could potentially be negated by a proper combination of the other two, and a combination of all three can negate any ambient or fuel perturbations. This work applies directly to the power block of an FC-GT hybrid in which recirculation can quickly adjust stack inlet temperature. Thus stack inlet temperature became a fourth parameter in the application of a control scheme to this FC model. Complete control of stack power output, average temperature, and temperature gradient, while maintaining high efficiency is achieved using these four control variables; power density, air flow, fuel utilization, and inlet temperature.

CONCLUSIONS

A dynamic model for high temperature fuel cell systems (SOFC and MCFC) was developed from first principles and found to exhibit expected system level behavior. Fuel to air ratio was shown to closely correlate with efficiency. Internal pre-heating, the novel modeling characteristic of this study, depends solely upon air flow rate regardless of operational conditions. This was likely due to boundary heat transfer being greater than the heat mobility within the stack. The importance of PEN temperature gradient as a control parameter could not be overstated, and depended heavily upon power density, inlet temperature, and air flow rate. MCFC systems responded favorably to increases in carbon dioxide concentration and fuel hydration for moderate steam to carbon ratios. Transient response emphasized the drastically different time scales between electrochemical outputs and thermal fluctuations. Novel control strategies have the potential to make use of the intermediate time scales for rapid transient response with small thermal fluctuations. Dynamic responses to step perturbations verified the utility of the model for future integration and dynamic control of high temperature fuel cell and hybrid fuel cell gas turbine systems.

ACKNOWLEDGMENTS

The authors thank the U.S. Department of Defense Fuel Cell Program and Mr. Frank Holcomb of the Construction Engineering Laboratory of the Engineer Research and Development Center for partial support of the current work under Contract Number W9132T-08-C-0003.

REFERENCES

[1] Hengeveld, D. W. (2007). Economic analysis of a combined heat and power molten carbonate fuel cell system. *Journal of Power Sources , 165*, 300-306.

[2] Cheekatamarla, P. K. (2009). Design, integration and demonstration of a 50 W JP8/kerosene fueled portable SOFC power generator. *Journal of Power Sources , 193*, 797-803.

[3] Marra, D. a. (2007). "Process analysis of 1 MW MCFC plant. *International Journal of Hydrogen Energy , 32*, 809-818.

[4] Rashidi, R. P. (2009). Performance investigation of combined MCFC system. *Journal of Hydrogen Energy* , 1-11.

[5] Bove, R. P. (2005). Experimental comparison of MCFC performance using three different biogas types and methane. *Journal of Power Sources , 145*, 588-593.

[6] Greppi, P. B. (2009). Feasibility of the integration of a molten carbonate fuel-cell system and an integraed gasification combined cycle. *International Journal of Hydrogen Energy , 34*, 8664-8669.

[7] Xu, J., & Froment, G. F. (1989). Methane Steam Reforming, Methanation and Water-Gas Shift: I. Intrinsic Kinetics. *AIChE Journal , 35* (1), 88-96.

[8] Sheng, M., Mangold, M., & Kienle, A. (2006). A strategy for the spatial temperature control of a molten carbonate fuel cell system. *Journal of Power Sources , 162*, 1213-1219.

[9] Brouwer, J., Jabbari, F., Leal, E. M., & Orr, T. (2005). Analysis of a molten carbonate fuel cell: Numerical modeling

and experimental validation. *Journal of Power Sources , 158*, 213-224.
[10] Fergus, J. W. (2006, November 8). Electrolytes for solid oxide fuel cells. *Journal of Power Sources* , 30-40.
[11] Kim, S., Yoon, S., Bae, J., & Yoo, Y.-S. (2009). Performance Analysis of CH4 Driven SOFC Short Stack. *Proceedings of FuelCell2009*, (pp. 1-7). Newport Beach.
[12] Winkler Wolfgang, H. L. (2002). Design studies of mobile applications with SOFC-heat engine modules. *Journal of Power Sources , 106*, 338-343.
[13] Mueller, F., Brouwer, J., Jabbari, F., & Samuelsen, S. (2006, May). Dynamic Simulation of an integrated Solid Oxide Fuel Cell System Including Current-Based Fuel Flow Control. (S. C. Singhal, Ed.) *Transactions of the ASME , 3*, pp. 144-153.
[14] Kaneko, T., Brouwer, J., & Samuelsen, G. (2006). Power and temperature control of fluctuating biomass gas fueled solid oxide fuel cell and micro gas turbine hybrid system. *Journal of Power Sources* , 316-325.
[15] Mueller, F., Jabbari, F., Brouwer, J., Roberts, R., & Junker, T. G.-A. (2009). Control design for a bottoming solid oxide fuel cell gas turbine hybrid system. *Journal of Dynamic Systems, Measurement, and Control* , 1-9.
[16] Roberts, R., Brouwer, J., Jabbari, F., Junker, T., & Ghezel-Avagh, H. (2006). Control design of an atmospheric solid oxide fuel cell/gas turbine hybrid system: Variable versus fixed speed gas turbine operation. *Journal of Power Sources* , 484-491.
[17] Mueller, F., Brouwer, J., Jabbari, F., & Samuelsen, G. (2006). Dynamic simulation of an integrated solid oxide fuel cell system including current-based fuel flow control. *Journal of Fuel Cell Science and Technology* , 144-155.
[18] Roberts, R., & Brouwer, J. (2006). Dynamic simulation of a pressurized 220 kW solid oxide fuel-cell-gas-turbine hybrid system: modeled performance compared to measured results. *Journal of Fuel Cell Science and Technology* , 18-25.